



Large-scale coupled hydrologic and hydraulic modelling of the Ob river in Siberia

Sylvain Biancamaria, Paul Bates, Aaron Boone, Nelly Mognard

► To cite this version:

Sylvain Biancamaria, Paul Bates, Aaron Boone, Nelly Mognard. Large-scale coupled hydrologic and hydraulic modelling of the Ob river in Siberia. *Journal of Hydrology*, 2009, 379 (1-2), pp.136-150. 10.1016/j.jhydrol.2009.09.054 . hal-00575483

HAL Id: hal-00575483

<https://hal.science/hal-00575483>

Submitted on 10 Mar 2011

HAL is a multi-disciplinary open access archive for the deposit and dissemination of scientific research documents, whether they are published or not. The documents may come from teaching and research institutions in France or abroad, or from public or private research centers.

L'archive ouverte pluridisciplinaire **HAL**, est destinée au dépôt et à la diffusion de documents scientifiques de niveau recherche, publiés ou non, émanant des établissements d'enseignement et de recherche français ou étrangers, des laboratoires publics ou privés.

Large-scale coupled hydrologic and hydraulic modelling of the Ob river in Siberia

Sylvain Biancamaria ^{a,*}, Paul D. Bates ^b, Aaron Boone ^c, Nelly M. Mognard ^a

Affiliations:

(a) Université de Toulouse; UPS (OMP-PCA); LEGOS; 14 Av. Edouard Belin, F-31400
Toulouse, France.

(b) School of Geographical Sciences, University of Bristol, University road, Bristol, BS8 1SS,
United Kingdom

(c) GAME/CNRM, Météo-France, CNRS, 42 Av. G. Coriolis, 31057 Toulouse Cedex, France

* Corresponding author. Tel.: +335 61 33 29 30; fax: +335 61 25 32 05. Email:

sylvain.biancamaria@legos.obs-mip.fr (S. Biancamaria)

Abstract

The Ob river in Western Siberia is one of the largest rivers in the Arctic and has a complex hydrological cycle mainly driven by snow melting in spring and rainfall and evapotranspiration in summer/autumn. The Ob is a source of fresh water for the Arctic Ocean and a change in its regime could affect the ocean thermohaline circulation. Due to the scarcity of in situ measurements in the Arctic and the size of the region, the hydrological modelling of large Arctic rivers is difficult to perform. To model the northern part of the Ob river basin, the land surface scheme ISBA (Interactions between Soil-Biosphere-Atmosphere) has been coupled with the flood inundation model LISFLOOD-FP. Different sensitivity tests on input data and parameters have been performed and the results have been compared with in-situ measurements and remotely sensed observations of water level. The best modelling is obtained with a river depth of 10 meters and a Manning coefficient of 0.015: correlation and Nash-Sutcliffe coefficients with in-situ measurement are equal or even slightly above (depending on the precipitation dataset used) 0.99 and 0.95 respectively. The sensitivity tests show that modelling errors are mainly linked with atmospheric input (snow and rain precipitation), snow cover and drainage parameterization for ISBA and Manning coefficient, river depth and floodplain topography for LISFLOOD-FP.

Keywords: arctic, Ob river, hydraulic-hydrologic modelling, ISBA, LISFLOOD-FP, GSWP2

1. Introduction

Global warming is expected to be most significant in the boreal regions and could greatly affect the discharge regime of arctic rivers (Meehl et al., 2007). The IPCC report, Meehl et al. (2007), stated that, for this century, temperature and precipitation in arctic regions will increase significantly. Already, an increase in arctic river flow has been observed by Peterson et al. (2002) and a modification in the arctic hydrological cycle could have a feedback on the whole climate through increased input of fresh water to the Arctic Ocean. However, since the early 1990's, the number of operational gauging stations has decreased markedly in the arctic, and especially for river basins located in the former USSR (Shiklomanov et al., 2002). For this reason the use of models and satellite measurement in conjunction with the few gauging station data sets still available is crucial to the ongoing study of arctic rivers to determine how they may respond to global warming. The purpose of this paper is to model the large scale hydrology and hydraulics of an arctic river using currently available data to identify where satellite measurements and models require improvement to address the above research questions. For this study the Ob river has been chosen as it is one of the biggest arctic rivers (the third largest in terms of discharge, Herschy and Fairbridge, 1998) and because it contributes nearly 15% of total freshwater flow into the Arctic Ocean (Grabs et al., 2000).

Previous attempts to model the hydrological cycle of arctic rivers have mostly used climate models applied at a regional and/or global scales. Such schemes can model the annual and seasonal flows at a basin scale (Decharme and Douville, 2007) and the global water fluxes at a regional scale (Su et al., 2006), or assess the influence of permafrost (Arzhanov et al., 2008) and artificial reservoirs on the global run-off (Adam et al., 2007). The main interest in using regional and global climate models is therefore their ability to estimate the effect of

global warming on the hydrology of the Arctic rivers (Nohara et al., 2006; Manabe et al., 2004) using the IPCC scenarios, however they cannot so easily be used to simulate how basin hydrology interacts with surface water flow through the river network and across complex floodplains. By contrast, there are very few attempts at modelling Arctic rivers using hydrodynamic models and these have been done for rivers smaller than the Ob, where it is easier to acquire in-situ data, such as the Peace-Athabasca Delta (Peters et al., 2006). For the Amazon, it has been shown that a hydrodynamic model can successfully model the river discharge and floodplain dynamics (Wilson et al., 2007) at regional scales. However, to the author's knowledge, the present study is one of the very first to model a large scale Arctic river with a coupled hydraulic-hydrologic model.

The paper is organised as follows. The study domain, the models and the input data used to simulate the hydrology of the Lower Ob river are presented in section 2. The results of the modelling and the sensitivity tests are described in section 3. Further improvements and perspectives on this work are discussed in the conclusions.

2. Methodology

2.1. Study domain and time period

The study domain corresponds to the Lower Ob River between the cities of Belogorje and Salekhard, which represents roughly the last 900 km of the river before the Ob estuary (Fig. 1) and corresponds to a drainage area of 790 000 km² (from the Arctic Rapid Integrated Monitoring System, ArcticRIMS, <http://rims.unh.edu>). The Ob river is located in Western Siberia, east of the Ural Mountains and its drainage basin covers 2 990 000 km². For discharge the Ob is the world's 12th biggest river and the 3rd biggest in the arctic (Hersch

and Fairbridge, 1998). Its discharge regime is mainly driven by snow melt and precipitation falling as rain between April and September and by rain precipitation from September to November. The strong relationship between spring discharge in May and snowmelt date and winter snow depth has been analysed using remote sensing techniques (Grippa et al., 2005; Yang et al., 2007). The study domain is classified as sporadic and discontinuous permafrost (Brown et al., 1998).

According to Serreze et al. (2002), precipitation in the Ob basin is at a maximum in summer. but is smaller than the evapotranspiration rate. Indeed, due to high evapotranspiration rates, about 25% of the July precipitation is associated with the recycling of water vapor evaporated within the domain, which shows the significant effect of the land surface (and therefore vegetation) on the summer hydrologic regime.

The Ob is frozen from November to April, and thawing occurs gradually during May (Pavelsky and Smith, 2004). During the thawing period some parts of the river can still be frozen, whilst the ice thawing in the most southern part creates ice jams further north which leads to widespread inundation, mainly at the tributary confluences (Pavelsky and Smith, 2004). Because the Ob is a “northward-flowing” river, the upper Ob ice cover breaks up around late April to May, whereas the break up occurs around late May to early June for the lower Ob (Yang et al., 2004). Especially, at Salekhard, near the Ob mouth, the river is covered with ice during 200 days per year in average and the spring ice break up happens approximately between May 20th and June 10th (Vuglinsky, 2001). Because of this delay in ice break up between the South and North parts of the basin, the lower Ob basin receives upstream runoff contribution and stores the flow in the main river valley above its mouth, resulting in widespread flooding in May over the northern parts of the Ob. According to Beltaos and Prowse (2008), ice flow produces significant hydrologic effects that often exceed in magnitude and frequency those occurring under open-water conditions. The impact of ice

jam is even more important as it occurs during the annual peak flow, leading to important erosive event (Prowse, 2001). Moreover, Smith and Alsdorf (1998) highlight that spring floods are a major source of sediment deposit in the Ob floodplain.

Analysis of monthly streamflow records for the major subbasins within the Ob river watershed during the 1936-1990 time period has been performed by Yang et al. (2004) to examine discharge changes induced by human activities and natural variations. Yang et al. (2004) found that over the upper Ob basin there is a decreasing streamflow trend for the summer months and an increasing streamflow trend during the winter season. The decreasing trend in summer is mainly due to water use along the river valley for agricultural and industrial purposes and because of reservoir regulation to reduce the summer peak floods. The increasing trend in winter streamflow is caused by reservoir management and the release of water for power generation. By contrast, in the lower Ob basin, streamflow increased during midsummer and winter months and weakly decreased in autumn. These increases in summer flow were associated with increases in summer precipitation and winter snow cover over the northern Ob basin. So according to Yang et al. (2004), human activity can significantly impact the Ob discharge for the upper basin, however this is not an issue for the study presented here as only the lower Ob has been considered. Here the impact of reservoir and human activity is already taken into account in the observed discharge data from the Belogorje gauging station (Fig. 1) which is used as boundary condition (i.e. as a proxy of the incoming discharge to our study domain from the upstream river).

The aim of the work presented here is to simulate a complex river system where the flow greatly depends on the correct simulation of snow accumulation during the winter and the onset of snow melt.

The study time period is 1993 as it corresponds to the year when the ISBA atmospheric inputs (1982-1994), the daily discharge measured at Belogorje (January 1993 -

October 1994) and the satellite altimetry data (since August 1992 up to now) are simultaneously available.

2.2. River model (LISFLOOD-FP)

The river is modelled by the flood inundation model LISFLOOD-FP developed at the University of Bristol (Bates and De Roo, 2000). It predicts water depth in each grid cell at each time step and hence can simulate the dynamic propagation of flood waves over fluvial, coastal and estuarine floodplains. LISFLOOD-FP is a coupled 1D/2D hydraulic model based on a raster grid. The 1D channel flow is based on the kinematic approximation to the 1D St Venant equations. Floodplain flows are similarly described in terms of continuity and momentum equations, discretized over a grid of square cells, which allows the model to represent 2-D dynamic flow fields on the floodplain. However there is no exchange of momentum between main channel and floodplain flows, only mass.

Fig. 2 shows all the data required to run LISFLOOD-FP. The main input data are the floodplain topography from a Digital Elevation Model (DEM) and the river centreline coordinates along with its width and depth. For this study the Manning coefficients for the river and for the floodplain have also been assumed constant in space and time. The incoming flow to the study domain from the upstream river is given by the daily discharge measured at the Belogorje gauging station (Fig. 1). The lateral inflows to the river in the study domain are computed by ISBA (Interactions between the Soil-Biosphere-Atmosphere, Noilhan and Mahfouf, 1996), which is a Land Surface Scheme (LSS) developed by the CNRM (Centre National de Recherche Meteorologique), see paragraph 2.3 for more detail. In this study, there are eight lateral inflows (Fig. 1). Finally, LISFLOOD-FP provides water height and discharge outputs for each point of the channel and for each grid cell on the floodplain.

2.3. Lateral inflows

Lateral inflows are a critical input for large area hydraulic models, and especially for arctic rivers where snow melt is the main driver of the river regime. They represent water from run-off and the drainage from the whole watershed to the river. Yet, no in-situ or remote sensing data are available to measure these contributions, so they can be estimated only by the combination of a LSS, which computes the surface water available at each grid cell of the basin and a routing scheme, which routes the surface water leaving each grid cell to the river. The next paragraphs present the LSS and the routing scheme used in this study.

2.3.1. ISBA

ISBA (Noilhan and Mahfouf, 1996) is a LSS with an explicit snow modelling component (Boone and Etchevers, 2001) and can simulate deep soil freeze-thaw cycles (Boone et al., 2000). Accurate snow pack modelling is of great importance to simulation of an arctic river and explain why ISBA has been chosen for this work. Moreover, ISBA has been used with the explicit soil diffusion option (Boone et al., 2000), which means the soil is explicitly modelled and is discretized into five layers with the highest vertical resolution at the surface. This option allows a more realistic simulation of the near-surface soil temperature gradient and freeze–thaw cycles than the classical force-restore option, see Boone et al. (2000) for more details. Moreover, the ISBA version used in this study includes a sub-grid runoff scheme (Habets et al., 1999).

Another key issue to estimate correctly the lateral inflows from ISBA to LISFLOOD-FP is the atmospheric data used as an ISBA input. In this study, forcing data comes from the

Global Soil Wetness Project – Phase II (GSWP2; Dirmeyer et al., 2006). GSWP2 aims to foster the development of LSSs and to assess the quality of their performance as well as that of the forcing datasets used to drive them. Therefore, different precipitation (rain and snow) datasets has been developed by GSWP2. These are based on two different reanalysis precipitation datasets: NCEP/DOE (Kanamitsu et al., 2002) and ERA-40 (Betts and Beljaars, 2003). Then, two corrections can be applied to these precipitation fields: hybridization (correction using gauge and satellite based precipitation data) and correction for gauge under-catch (Dirmeyer et al., 2006). For the first correction (hybridization), two observational precipitation datasets can be used: the gauge-based Global Precipitation Climatology Centre (GPCC, Rudolf et al., 1994) and the satellite-based Global Precipitation Climatology Project (GPCP, Huffman et al. 1997), leading to different hybridization corrections (Dirmeyer et al., 2006). GSWP2 has defined several experiments by combining the two precipitation datasets with the different corrections (Table 1). Decharme and Douville (2006) compared multi-model outputs forced with GSWP2-B0 and GSWP2-P3 on the French part of the Rhône river basin. Compared to an observation-based dataset, they concluded that GSWP2-P3 gives better results than GSWP2-B0. For this reason in this study the GSWP2-P3 forcing field has been used for the nominal run.

ISBA was run with the same $1^{\circ} \times 1^{\circ}$ spatial resolution as the GSWP2 forcing data and used to compute the run-off (surface water) and drainage (sub-surface water) leaving each $1^{\circ} \times 1^{\circ}$ grid cell. Yet, as each ISBA grid cell is spatially independent and not coupled laterally with any other, a routing scheme is required to bring to the river the water which leaves each pixel.

2.3.2. Routing Scheme

The routing scheme used to route the run-off and drainage from each ISBA pixel to the river is the Total Runoff Integrating Pathways (TRIP; Oki and Sud, 1998) algorithm. TRIP is a global river channel network at $1^{\circ} \times 1^{\circ}$ resolution, extracted from the ETOPO5 DEM and publicly available from <http://hydro.iis.u-tokyo.ac.jp/~taikan/TRIPDATA/>. TRIP gives the flow direction from each pixel with the three following constraints:

1. No river channels are allowed to cross.
2. All river channels flow from one land grid box to another.
3. Every land grid box has one, and only one, river mouth toward its downstream.

Fig. 3 shows the routing scheme derived from TRIP to route the water computed from each ISBA pixel within the drainage area to an ISBA pixel which contains a segment of the lower Ob (blue dots on the Fig. 3). These amounts of water represent the lateral inflows to the river computed from ISBA+TRIP. Finally, each lateral inflow is inserted as a point source into LISFLOOD-FP at the point along the river vector which is closest to the center of the blue ISBA grid cells in Fig. 3 (i.e. the whole model unit is assigned to one point along the LISFLOOD-FP reach).

2.4. Ancillary data

2.4.1. Gauge data

In this study discharge from two gauging stations are used (see Fig. 1 for their location). The first one, at Belogorje, is used to estimate the incoming upstream flow to the study domain. The second one at Salekhard is used to validate the modelled discharge. Discharge time series for these two gauging stations have been downloaded from the ArcticRIMS website (<http://rims.unh.edu>).

2.4.2. Channel topography and parameters

The river centreline has been extracted from the CIA World Data Bank II river mask (Gorny and Carter, 1987). From this river vector, it has been estimated that the average distance along the river between two lateral inflows is around 140 km. However the river depth and width are not well known along the river. From Landsat images, the mean river width for the Lower Ob is around 2 km, yet with large variability at some locations. Thus, the river width along the Ob has been considered constant and equal to 2 km (two pixels of the floodplain topography, see section 2.4.3). A previous study from Akimenko et al. (2001) stated that maximum depths on the lower Ob can reach 15m to 20m. To estimate the channel topography, it has been assumed that river bed elevation corresponds to the smoothed DEM elevation along the river centre minus a constant river depth (Fig. 4). To test the uncertainty in the river depth, four different values (5m, 10m, 15m and 20m) of river depth have been used and simulations run with each of these.

The Manning coefficient (or friction coefficient) for the river is not well known, however for a river channel with a sand bed and no vegetation the Manning coefficient is known to vary from 0.011 to 0.035 (Chow, 1964). So, to simplify the modelling, the channel Manning coefficient has been set to a constant value in space and time and several runs have been done with different plausible value (from 0.01 to 0.04 in steps of 0.005).

2.4.3. Floodplain topography and parameters

For high latitudes very few DEMs are available. The best ones are ACE (Altimeter Corrected Elevation) from De Montfort University and GTOPO30 from the USGS (United

States Geological Survey). Both have a 30 arc-seconds (~1km) spatial resolution, which is therefore the LISFLOOD-FP output spatial resolution. Yet, after plotting the two DEM (Fig. 5), it becomes obvious that they have artefacts which will greatly affect the simulated floodplain inundation. Indeed, on the study domain below 66°N, ACE has been generated by interpolating ERS-1 data from its geodetic mission. Above 66°N, it uses the same data as GTOPO30. Fig. 5a shows the interpolation artefacts (where the satellite ground tracks can be seen). For GTOPO30, the data come from different Digital Terrain Elevation Data (DTED), with different resolutions and qualities. This is why sometimes there is an obvious offset due to change of data sources, as is clearly shown in Fig. 5a around 64°N. Because of these offsets and because GTOPO30 has a constant value in the river floodplain between 62.3°N and almost 64°N (Fig. 5a), using this DEM gives non realistic floodplain water depths in the LISFLOOD-FP model (Biancamaria et al., 2007). For these reasons the ACE DEM has been chosen for our modelling as it represents the best of the poor terrain datasets available. The Manning coefficient for the floodplain has been assumed constant in space and time and equal to 0.06.

2.4.4. ISBA vegetation parameters

In this study the vegetation and soil parameters (Leaf Area Index (LAI), Vegetation cover fraction, non-snow-covered surface all-wavelength albedo and non-snow-covered bare soil-vegetation roughness length) used as input to ISBA come from Ecoclimap (Masson et al., 2002). Ecoclimap is a monthly global surface parameter dataset at 1-km resolution and has been derived by combining existing land cover and climate maps, in addition to using Advanced Very High Resolution Radiometer (AVHRR) satellite data. This dataset has been resampled at 1°x1° spatial resolution for the study domain.

Another vegetation cover and LAI dataset, from the University of Wales, is also available and has been used by GSWP2. It has been computed from Pathfinder Advanced Very High Resolution Radiometer (AVHRR) Land (PAL) channel 1 and 2 data, and corrected for Bidirectional Reflectance Distribution Function (BRDF) effects, volcanic aerosols, cloud and atmospheric effects and missing data. This dataset has a monthly time resolution and is available for the years 1982 to 1998. This second set of vegetation data has been used in this study to investigate the sensitivity of the modelling to the vegetation parameters.

3. Results and sensitivity tests

The hydrology of the Ob basin, as modelled by ISBA, is first described and issues with modelled lateral inflows are discussed and investigated. Sensitivity to ISBA vegetation and drainage parameters, and to precipitation input is studied in section 3.1. Sensitivity to LISFLOOD-FP parameters, like river depth and Manning coefficient, is addressed in section 3.2. Lastly, model validation for a nearly ungauged river like the Ob is a very tricky task. For this reason the chosen model validation strategy is as follow: modelled outputs from ISBA/LISFLOOD-FP are first compared to in-situ measurement and then water elevations modelled by LISFLOOD-FP are compared to Topex/POSEIDON data.

3.1. Sensitivity to ISBA inputs and parameters

3.1.1. Modelled Ob basin hydrology

Based on energy budgets and parameterization of physical processes, ISBA modelled the physical hydrology of the lower Ob. In particular, the use of a three layers snow scheme

and an explicit five layers soil, with a freezing module (allowing modelling of permafrost conditions), is well suited to simulation of high latitude hydrology. Since ISBA is used to compute the lateral inflows to the river, its value can be validated by a simple computation of the difference between the measured discharge at the Belogorje and Salekhard gages. Yet, as there are 900km between Belogorje and Salekhard, there is a time lag between the two measured discharges. The computation of the cross-correlation between measured time-series at Belogorje and at Salekhard shows that the peak discharge at Belogorje occurs 10 days before the peak discharge at Salekhard (Fig. 6a). The difference between Salekhard discharge and a 10 days-time-lag Belogorje discharge shows that the total lateral inflows between the two gages has a maximum value of 12 000 m³/s occurring between the end of May and the beginning of June (Fig. 6a and 6b). However, the sum of all the lateral inflows modelled by ISBA has a maximum of 8 000 m³/s and occurs between the end of March and the beginning of April (fig 6b). Therefore, the peak in modelled lateral inflows is not only underestimated but occurs almost two months in advance compared to in-situ measurements. Fig. 6c shows the modelled discharge time-series for each lateral inflow. There are three predominant lateral inflows: lateral inflow numbers 2, 6 and 8 (see Fig. 3 for their location). Whilst these all have a discharge maximum at the end of March, lateral inflow n°6 is the major contributor to the peak in the sum of all the modelled lateral inflows which occurs during the March/April period.

To investigate the cause of this early modelled lateral inflows, different hydrological variables modelled by ISBA have been plotted on Fig. 7. All the plots on this figure correspond to spatial averages over all the ISBA grid cells contributing to lateral inflow n°6 (see Fig. 3 for the location of these grid cells). For the year 1993, rain precipitation mostly occurs between June and October (Fig. 7a), with a mean value of 0.9 mm/day and a maximum value of 11 mm/day. Snow precipitation occurs from January to May and September to

December 1993 (Fig. 7b), with a mean value of 0.9 mm/day and a maximum value of 6.5 mm/day. The evapotranspiration (Fig. 7c) is important in summer (between June and September) with a mean value of 1.6 mm/day and a maximum value of 3.9 mm/day (during this period the mean rain precipitation rate is just a bit smaller than 1.6 mm/day). During the rest of the year, evapotranspiration is very small. These results are quite similar, yet slightly lower, than the ones from Serreze et al. (2002) for the entire Ob basin (precipitation rate of 1.9 mm/day and evapotranspiration of 2 mm/day in summer). Surprisingly, snow fraction (Fig. 7d), which is the fraction of snow covering a grid cell, is very small and never exceeds 0.17. This means that less than 17% of the area of each grid cell contributing to lateral inflow is covered by snow during winter time. This is due to the ISBA sub-grid snow fraction parameterization, which considers that the snow cover fraction generally stays relatively low when tall vegetation is present, in order to represent vegetation elements protruding through the snowpack. This small snow fraction has two effects: first, soil is not isolated from the air temperature during winter and second, the albedo of the surface is lower and so it can be warmed more rapidly by incoming solar radiation. Therefore, modelled temperature in the first soil layer (Fig. 7f) is almost exactly the same as the as air temperature (Fig. 7e). Thus, when air temperature rises in March and becomes above 0°C for 5 consecutive days, ground temperature rapidly acquires the same value, leading to the melt of nearly all the snowpack in March. Finally, Fig. 7g and 7h present the total liquid water equivalent soil ice and soil liquid water content, respectively. Contrary to snow, soil ice barely decreases during mid-March when soil temperature becomes above 0°C for a few days. Soil ice content really begins to decrease in mid-April, when soil temperature is equal or above 0°C for a longer period and when there is almost no more snow to absorb heat. Soil ice completely disappears between July and September. Soil water content, which is small in winter, increases rapidly during mid-March snow melt and after mid-April, with two local maxima in July and October.

3.1.2. Sensitivity to the snow fraction parameters

The discharge peak in March in the modelled lateral inflows is mainly due to an early snow melt caused by a small snow fraction modelled by ISBA. The total snow fraction (p_n) computed by ISBA is a weighted sum (Eq. 3) of the snow fraction over vegetation (p_{nc} , Eq. 1) and over bare soil (p_{ng} , Eq. 2), see Pitman et al. (1991) for more information about Eq. (1) and Eq. (2).

$$p_{nc} = \left(\frac{D_S}{D_S + c_{pn} Z_0} \right)^{b_{pn}} \quad (0 \leq p_{nc} \leq 1) \quad (1)$$

$$p_{ng} = \left(\frac{W_S}{a_{pn} W_S + W_{np}} \right)^{b_{pn}} \quad (0 \leq p_{ng} \leq 1) \quad (2)$$

$$p_n = (1 - veg) \cdot p_{ng} + veg \cdot p_{nc} \quad (3)$$

where D_s is the snow depth computed by ISBA, W_s is the snow water equivalent (SWE) computed by ISBA, W_{np} is the generalized critical SWE ($W_{np}=10 \text{ kg.m}^2$), $a_{pn}=1$, $b_{pn}=1$, $c_{pn}=5$, Z_0 is the soil/vegetation roughness length and veg is the vegetation fraction cover. This is a fairly standard sub-grid parameterization which was developed for use in large scale General Circulation Model (GCM) applications (see Wu and Wu, 2004, for a review of such schemes).

Z_0 and the vegetation cover are climatological monthly varying ISBA inputs. The mean value of the vegetation cover (from ECOCLIMAP) for all the grid cells contributing to lateral inflow 6 is equal to 0.94 (Fig. 8a). In ECOCLIMAP, those grid cells are classified as forest, and consequently Z_0 is relatively high (between 1.32 and 1.36 m). This means that, given the value of Z_0 , snow fraction over vegetation is quite small (around 0.15, Fig. 8b) and,

because vegetation cover is close to 1, the total snow fraction is almost equal to the snow fraction over vegetation (Eq. 3), which explains the small value of the total snow fraction. There are two solutions to this issue: 1- vegetation fraction cover is not realistic and should be decreased and/or 2- the snow fraction of vegetation is not realistic and should be increased. Solution 1 does not seem to be the most likely, as the vegetation cover is based on actual satellite data. To test the sensitivity of the modelling to the vegetation cover, vegetation parameters from ECOCLIMAP have been replaced by the dataset from the University of Wales (see section 2.4.4). Yet, modelled lateral inflows were still very similar, with an early snowmelt in March. By contrast, solution 2 might be the most likely, because there is more uncertainty in the parameterization of p_{nc} . Indeed, from Eq. (1) it is clear that snow fraction over vegetation is a function of SWE and Z_0 , whereas snow fraction over bare soil (Eq. 2) is only a function of SWE (or snow depth). The basic idea behind this parameterization is that bare ground is more quickly covered with snow than areas with high vegetation (like forests). Thus, if Z_0 is high, as it is the case here, snow fraction over vegetation will be low. Yet, this behavior depends on the coefficients in Eq. (1) and especially c_{pn} . Even if Eq. (1) and Eq. (2) are commonly used by LSSs like ISBA, the value of their coefficients is very empirical with huge uncertainties and therefore is highly variable between different models (Pitman et al., 1991; Verseghy, 1991; Yang et al., 1997). Thus, the c_{pn} coefficient can be tuned to obtain a better timing in the modelled snow melting.

The high value of Z_0 might not be completely realistic when there is snow. Indeed, pure snow has a very small roughness length, around 0.001 m. So, the “true” roughness length of a grid cell should be reduced when there is snow. A simple way to take this physical process into account is to do a nonlinear average of a snow roughness for a pure snow surface and the initial value of Z_0 (Eq. 4 and Eq. 5). This kind of average is commonly used for roughness length computation (Noilhan and Lacarrère, 1995).

$$Z_{0n} = p_n \frac{1}{\left[\ln \left(\frac{0.001}{P_{zref}} \right) \right]^2} + (1 - p_n) \frac{1}{\left[\ln \left(\frac{Z_0}{P_{zref}} \right) \right]^2} \quad (4)$$

418

$$Z_{0new} = P_{zref} \cdot \exp \left(\frac{-1}{\sqrt{Z_{0n}}} \right) \quad (5)$$

420 Fig. 9 shows the lateral inflows computed from ISBA for c_{pn} equal to 5 (nominal
 421 value), 1, 0.1, 0.01 and 0.001, for a roughness length equal to Z_0 (Fig. 9a) and to Z_{0new} (Fig.
 422 9b). The higher the values of the c_{pn} coefficient yield, the better the timing of the modelled
 423 lateral inflow sum. Yet, the maximum modelled total inflow can be very high and the base
 424 flow is still very low. For Z_{0new} , increasing c_{pn} above 0.01 does not significantly change the
 425 total lateral inflow. Besides, total lateral inflow with Z_{0new} and c_{pn} equal to 0.01 is very close
 426 to lateral inflow with Z_0 and c_{pn} equal to 0.001. Now that total lateral inflow has a good
 427 timing, it is necessary to increase the base flow and reduce the maximum discharge.

428

429 3.1.3. Sensitivity to drainage parameter

430

431 From Fig. 9, it is obvious that modelled lateral inflows' base flow is too small. In
 432 ISBA a parameterization has been implemented which allows the model to generate drainage
 433 or base flow even over dry soil (Etchevers et al., 2001). It assumes that when the soil water
 434 content is below a given threshold (called w_{drain} , in m^3/m^3), the drainage is constant at a rate
 435 based on the soil texture. However, this means that there will be less water flow during wet
 436 periods. When w_{drain} is equal to 0 (like in the nominal version of ISBA used up to now) this
 437 parameterization is disabled. Fig. 10 shows the sum of all lateral inflows for $c_{pn}=0.01$,
 438 roughness length equal to Z_{0new} and w_{drain} equal to 0, 0.01, 0.02, 0.03 and 0.05. Clearly, for

w_{drain}>0.02, base flow is too high and the maximum discharge is too small. For w_{drain} equal to 0.01 and 0.02, globally base flow seems in good agreement with in-situ measurement, except during November and December when it is overestimated. For w_{drain} equal to 0.01, maximum discharge is still overestimated and delayed by a few days. On the contrary, for w_{drain} equal to 0.02, maximum discharge is slightly underestimated, but still delayed compared to the difference between in-situ discharge at Salekhard and Belogorje. However, no matter the value of w_{drain}, the total lateral inflow is always underestimated between July and August. This might due to too weak rain precipitation used as ISBA input and/or because ISBA does not model aquifer or local perched water tables, which contribute to river flow during the dry season.

3.1.4. Sensitivity to precipitation input

Fig. 11 shows the sum of all lateral inflows modelled by ISBA forced by the six precipitation datasets available from GSWP2 (see section 2.3.1 and Table 1) with $c_{pn}=5$, w_{drain}=0 and Z_0 (nominal run, a.) and with $c_{pn}=0.01$, w_{drain}=0.02 and Z_{0new} (b.). B0 and P2 give similar results and greatly overestimate total lateral inflow. P4 is very similar to PE, but they are both smaller than B0 and P2, even if they still underestimate total lateral inflow. On the contrary, GSWP2-P1 and P3 are comparable and underestimate total lateral inflow. Therefore, it appears that there is a lot of variability in the modelled lateral inflows, depending on the precipitation datasets. Yet, the difference between in-situ measurements at Salekhard and Belogorje is just a rough estimate of the total lateral inflow and for a real assessment of the “best” precipitation dataset to use, it is necessary to compare the modelled discharge at Salekhard and the in-situ measurement (fig11.c and d). The modelled discharge at Salekhard is obtained for a 10 m river depth and a Manning coefficient of 0.015 (see next

section for a sensitivity study to these parameters). Discharge is modelled for all GSWP2 precipitation datasets using two groups of parameters: 1) $c_{pn}=5$, $w_{drain}=0$ and Z_0 (fig 11.c) and 2) $c_{pn}=0.01$, $w_{drain}=0.02$ and Z_{0new} (fig 11.d). As expected, for all precipitation datasets lateral inflows computed with $c_{pn}=0.01$, $w_{drain}=0.02$ and Z_{0new} are in better agreement with the difference between measured discharge at Salekhard and Belogorje than lateral inflow obtained with $c_{pn}=5$, $w_{drain}=0$ and Z_0 . Table 2 presents the correlation coefficient, bias, Root Mean Square Error (RMSE) and Nash-Sutcliffe coefficient between observed and modelled discharge at Salekhard for all precipitation fields. The best results are obtained with GSWP2-P1 and P3, even if they underestimate discharge. GSWP2-P4 gives fairly good results but overestimates discharge. The worst results are obtained for GSWP2-B0 and P2 which dramatically overestimate discharge. This is coherent with the work from Decharme and Douville (2006), who also found that modelled discharge is greatly overestimated when applying correction for gauge under-catch to hybridized precipitation dataset. Moreover, they found that discharge modelled using GSWP2-P3 precipitation field is always underestimated at high latitude, which is confirmed here.

From these results, lateral inflows obtained with GSWP2-P3 and P4 (which are quite different but still close to in-situ measurement) and $c_{pn}=0.01$, $w_{drain}=0.02$ and Z_{0new} will be used for the sensitivity study to LISFLOOD-FP parameter in the next section.

3.2. Sensitivity to LISFLOOD-FP parameters

3.2.1. Sensitivity to river depth and Manning coefficient

As LISFLOOD-FP assumes a rectangular channel cross section, the river depth determines the maximum discharge in the main river channel and when there will be

inundation. The river width plays the same role, and for this reason, to simplify the sensitivity tests, only river depth is changed. Since the Ob river depth can reach 15m and even 20m, three different values of the constant river depth (5m, 10m and 15m) have been tested. As river depth decreases, so does the capacity of the channel and more water is transferred to floodplain sections during high discharge events. This increased floodplain storage has the effect of delaying the downstream progression of the flood wave.

The Manning coefficient greatly impacts the flow speed, which then impacts discharge and flood extent. Indeed, the slower the flow, the more water can be accumulated and then be available for floodplain inundation. The Ob bed is mainly composed of sand (Akimenko et al., 2001) and the lower Ob is mostly a straight river, so the Manning coefficient can be chosen to be about 0.02 (Chow, 1964). Yet, at some periods of the year it can increase, for example during snow melt when the river carries ice and mud. For this reason the model has been run for four values of the channel Manning coefficient (0.01, 0.015, 0.020 and 0.025).

Fig. 12a and 12c present, respectively for GSWP2-P3 and GSWP2-P4 lateral inflows, the modelled discharge at Salekhard for different values of river depth (red and magenta curves) for a Manning coefficient of 0.015. On these plots, the blue curve corresponds to the measured discharge at Salekhard. These plots clearly show that for greater river depth the maximum discharge happens earlier, with a higher amplitude, than for smaller river depth. For river depths equal or above 10m, there is a good timing between modelled and in-situ discharge, for both precipitation datasets. This good agreement is mainly due to limited overbank flooding leading to attenuation of the flood wave.

Fig. 12b and 12d present, respectively for GSWP2-P3 and GSWP2-P4 lateral inflows, the modelled discharge at Salekhard for different values of the Manning coefficient (red and magenta curves) for a river depth of 10m. The different curves clearly show that, with a

higher channel Manning coefficient, the water is slowed down, which could increase floodplain inundation and delay the modelled discharge.

Furthermore, for both precipitation forcing fields, there is a delay between in-situ and modelled discharges between September and December, when discharge is only driven by autumn rainfall. This delay is difficult to explain and could be due to a wide range of reasons: errors in the precipitation location (for example if the location of rainfall in the GSWP2 data set is further south, then it will take more time for the water to reach Salekhard) or in the timing, a change in the value of the friction coefficient (in spring the friction should be higher because of ice melting, yet the Manning coefficient is already very low), etc.

To find the best couples of LISFLOOD-FP parameters (Manning coefficient and river depth), the mean error, root mean square error, correlation coefficient and Nash-Sutcliffe coefficient have been computed (Table 3) between observed and modelled discharge for each value of the Manning coefficient and river depth (for both GSWP2-P3, normal size numbers, and GSWP2-P4, bold numbers). For GSWP2-P3, the best agreement between observed and modelled discharge is obtained with a river depth of 15m and a Manning coefficient of 0.020 (the RMSE is minimized and equal to 1 956 m³/s). However, for GSWP2-P4, the best agreement between observed and modelled discharge is obtained with a river depth of 10m and a Manning coefficient of 0.015 (the RMSE is minimized and equal to 2 409 m³/s).

These values of the parameters seem reasonable for a river channel with a sand bed and no vegetation (the Manning coefficient is known to vary from 0.011 to 0.035, Chow, 1964) and with a maximum river depth between 15m or 20m (Akimenko et al., 2001).

3.2.2. Comparison with altimetry

To estimate which averaged river depth between 10m and 15m is closer to reality, the modelled water elevations along the river channel have been compared to measured water elevations from the Topex/POSEIDON satellite radar altimeter. The location of the twenty two Topex/POSEIDON virtual stations used in this study is shown by the red dots on Fig. 13. As the lower Ob is wide (river width is around 2 km), the altimeter gives relatively good results, except in winter, when the river is frozen. For this reason the comparison between modelled and remotely sensed water heights has only been undertaken for the period May to September 1993. Whilst the ability of the LISFLOOD-FP model to match these data will be hampered by errors in the floodplain DEM, this should give some indication as to which river depth is most likely to be correct.

Fig. 14 shows the comparison between the height measured by Topex/POSEIDON (red curve) and the modelled height with GSWP2-P3 (magenta dashed curve) and with GSWP2-P4 (black curve) for a 10 m river depth and a 0.015 Manning coefficient at the location of Topex/POSEIDON measurements n°4 (a.), n°9 (b.), n°17 (c.) and n°24 (d.), see Fig. 13 for their location. Water heights modelled with GSWP2-P4 appear to be closer to the satellite measurement than water heights modelled with GSWP2-P3. This is due to the fact that total lateral inflow computed by ISBA using GSWP2-P4 precipitation dataset is higher than total lateral inflow obtained with GSWP2-P3. In particular, with GSWP2-P3, lateral inflow n°2 is quite small compared to lateral inflow n°6 and 8, which is not the case with GSWP2-P4, (lateral inflow n°2 has the same order of magnitude as the two other lateral inflows). Furthermore, there is no significant phase error between modelled and measured water heights.

Table 4 shows the mean RMSE between Topex/POSEIDON and modelled water heights for all Topex/POSEIDON stations and the four stations shown in Fig. 14, for the two best couples of river depth and Manning coefficient found in section 3.2.1 for GSWP2-P3 and

GSWP2-P4. Table 4 confirms the better agreement between Topex/POSEIDON and modelled water elevation for GSWP2-P4. The RMSE between altimetry measurements and modelled water heights increased with latitude especially above 65°N, which means that either the hypothesis of a constant river depth is not realistic or that the switch in the ACE DEM at 66°N to use the GTOPO30 data degrades the ability of LISFLOOD-FP to predict water surface elevation. In addition, the hypothesis that each lateral inflow computed by ISBA is inserted as a single point source into LISFLOOD-FP might also explain why some RMSEs are smaller than others. In reality, a single ISBA lateral inflow might correspond to different tributaries which do not reach the main stream at the same point. Therefore, modelled water height may be different from the true one, even if channel bathymetry was perfectly known.

For both precipitation datasets, it appears that the best prediction of large scale flow hydraulics is obtained by using a river depth around 10m and a Manning coefficient of 0.015.

4. Conclusions and perspectives

This study shows that it is possible to model discharge of a nearly ungauged arctic basin by coupling a hydrologic (ISBA) and a hydrodynamic (LISFLOOD-FP) model using simple assumptions for river parameters (constant Manning coefficient and river depth) and in-situ measurements as a proxy for the upstream flow. Different sensitivity tests on input data and parameters show that the modelling is sensitive to the atmospheric input (rain and snow precipitation), snow cover and drainage parameterization for ISBA, and to Manning coefficient and river depth for LISFLOOD-FP. The DEM is a key parameter in the discharge uncertainty as it controls floodplain water depths, hydroperiod and storage volume, which in turn influences wave propagation speeds (Biancamaria et al., 2007). The study presented here used different precipitation datasets from GSWP2 to model the lower Ob river. Best results

are obtained with precipitation fields which are not corrected from gauge under-catch and in particular with GSWP2-P3 and GSWP2-P4 datasets. This finding is in agreement with a previous study from Decharme and Douville (2006). Furthermore, it has been shown that a change in the value of two ISBA parameters driving soil drainage and the snow fraction over vegetation respectively, allows a better timing and amplitude of the modelled lateral inflows to the river. Comparison with in-situ measurements at the exit of the study domain and observed water heights from Topex/POSEIDON along the river has allowed to estimate the best value of the LISFLOOD-FP river depth (10 m) and Manning coefficient (0.015). With GSWP2-P3 precipitation, a 10 m river depth and a Manning coefficient of 0.015, the correlation coefficient and RMSE between modelled and observed discharge at the exit of the study domain are respectively equal to 0.99 and 1917 m³/s (which represents 14% of the mean in-situ discharge). With GSWP2-P4 precipitation and the same value of the river parameters, the correlation coefficient and RMSE between modelled and observed discharge at the exit of the study domain are respectively equal to 0.99 and 2289 m³/s (which represents 17% of the mean in-situ discharge). The RMSE between modelled and Topex/POSEIDON measured water heights along the river is equal to 2.6 m and 2.0 m for GSWP2-P3 and GSWP2-P4 respectively. Yet, the value of the RMSE is relatively dependent of the location along the river.

The sensitivity of the modelling to the different parameters is a key factor and since there are only sparse in situ measurements, satellite estimates should be used in the future to refine some of the models parameters such as the Manning coefficient, drainage parametrization, etc to improve the models and simulate how basin hydrology interacts with surface water flow through the river network and across complex floodplains. This could be done by assimilating these satellite data both in ISBA and LISFLOOD-FP. In particular, this kind of study will greatly benefit from future wide swath altimetry, like the Surface Water and

612 Ocean Topography (SWOT) mission, planned for launch around 2013/2016. SWOT will
613 measure 2D water heights over a 120 km wide swath and thus better constrain the models
614 (compared to 1D measurements from nadir altimetry or in-situ measurements).

615 Finally, undertaking this type of modelling is inherently difficult as the studied
616 processes are poorly known and interact in a complex manner. This study is one of the first to
617 investigate the hydrodynamic modelling of the lower Ob and the results are promising. This
618 work therefore provides a significant contribution to the understanding of modelling for a
619 large Arctic river basin and offers new and promising perspectives.

620 Acknowledgements

621

622 The authors are greatly thankful to the ArcticRIMS project for their huge work to gather and

623 to freely distribute gauging data for the arctic regions via their website (<http://rims.unh.edu>).

624 They are also very grateful to Pr. Taikan Oki for letting TRIP data freely available for

625 download on his website (<http://hydro.iis.u-tokyo.ac.jp/~taikan/TRIPDATA/>).

626 Moreover, they are grateful to Frederic Frappart for providing the Topex/POSEIDON data.

627 The GSWP2 team is acknowledged for letting the authors use their different forcing fields.

628 The authors also wish to thank one anonymous reviewer who made comments which

629 significantly improved this paper.

630 All the maps have been drawn using the General Mapping Tools.

631 This work has benefited from funding by the ANR, IMPACT BOREAL, and the IPY CARE

632 projects, one of the authors (S. Biancamaria) is supported by a CNES/Noveltis grant.

633

References

- Adam, J.C., Haddeland, I., Su, F.G., Lettenmaier, D.P., 2007. Simulation of reservoir influences on annual and seasonal streamflow changes for the Lena, Yenisei, and Ob' rivers. *Journal of Geophysical Research-Atmospheres* 112, D24.
- Akimenko, T.A., Zakharova, E.A., Kouraev, A.V., 2001. Hydrology of the Ob' river system. Working Paper, INTAS Project 97-3127.
- ArcticRIMS, <http://rims.unh.edu>.
- Arzhanov, M.M., Eliseev, A.V., Demchenko, P.F., Mokhov, I.I., Khon, V.C., 2008. Simulation of thermal and hydrological regimes of Siberian river watersheds under permafrost conditions from reanalysis data. *Izvestiya Atmospheric and Oceanic Physics* 44(1), 83-89.
- Bates, P.D., De Roo, A., 2000. A simple raster-based model for floodplain inundation. *Journal of Hydrology* 236, 54-77.
- Beltaos, S., Prowse, T., 2008. River-ice hydrology in a shrinking cryosphere. *Hydrological Processes* 23, 122-144.
- Betts, A.K., Beljaars, A.C.M., 2003. ECMWF ISLSCP-II near surface dataset from ERA-40. ERA-40 Project Report Series 8, [Available from the European Centre for Medium Range Weather Forecasts, Shinfield Park, Reading, Berkshire RG2 9AX, England], 31 pp.

659

660 Biancamaria, S., Bates, P.D., Boone, A., Mognard, N., Crétaux, J.-F., 2007. Modelling the Ob
661 river, in western Siberia, using remotely sensed digital elevation models. Proceedings of the
662 « Second Space for Hydrology Workshop », Geneva, 12-14 November 2007, ESA Workshop
663 Proceedings Publication WPP-280.

664

665 Boone, A., Masson, V., Meyer, T., Noilhan, J., 2000. The Influence of the Inclusion of Soil
666 Freezing on Simulations by a Soil-Vegetation Atmosphere Transfer Scheme. Journal of
667 Applied Meteorology 39, 1544-1569.

668

669 Boone, A., Etchevers, P., 2001. An Intercomparison of Three Snow Schemes of Varying
670 Complexity Coupled to the Same Land Surface Model: Local-Scale Evaluation at an Alpine
671 Site. Journal of Hydrometeorology 2, 374-394.

672

673 Brown, J., Ferrians Jr., O.J., Heginbottom, J.A., Melnikov, E.S., 1998 (revised February
674 2001). Circum-Arctic map of permafrost and ground-ice conditions. Boulder, CO: National
675 Snow and Ice Data Center/World Data Center for Glaciology, Digital Media.

676

677 Chow, V.T., 1964. Handbook of Applied Hydrology. McGraw-Hill Book Company, New-
678 York, USA.

679

680 Decharme, B., Douville, H., 2006. Uncertainties in the GSWP-2 precipitation forcing and
681 their impacts on regional and global hydrological simulations. Climate Dynamics 27, 695–
682 713.

683

684 Decharme, B., Douville, H., 2007. Global validation of the ISBA sub-grid hydrology. *Climate*
 685 *Dynamics* 29(1), 21-37.
 686
 687 Dirmeyer, P.A., Gao, X., Zhao, M., Guo, Z., Oki, T., Hanasaki, N., 2006. GSWP-2:
 688 Multimodel Analysis and Implications for Our Perception of the Land Surface. *Bulletin of the*
 689 *American Meteorological Society*, 87, 1381–1397.
 690
 691 Etchevers, P., Golaz, C., Habets, F., 2001. Simulation of the water budget and the river flows
 692 of the Rhône basin from 1981 to 1994. *Journal of Hydrology* 244, 60-85.
 693
 694 Gorny, A.J., Carter, R., 1987. *World Data Bank II General User's Guide*. Central Intelligence
 695 Agency, Washington, DC, USA.
 696
 697 Grabs, W.E., Fortmann, F., De Couuel, T., 2000. Discharge observation networks in Arctic
 698 regions: Computation of the river runoff into the Arctic Ocean, its seasonality and variability.
 699 *The Freshwater Budget of the Arctic Ocean*, E. L. Lewis et al., Eds., Kluwer Academic, 249–
 700 268.
 701
 702 Grippa, M., Mognard, N., Le Toan, T., 2005. Comparison between the interannual variability
 703 of snow parameters derived from SSM/I and the Ob river discharge. *Remote Sensing of*
 704 *Environment* 98, 35-44.
 705
 706 Habets, F., Noilhan, J., Golaz, C., Goutorbe, J.P., Lacarrère, P., Leblois, E., Ledoux, E.,
 707 Martin, E., Ottlé, C., Vidal-Madjar, D., 1999. The ISBA surface scheme in a macroscale

708 hydrological model applied to the HAPEX-MOBILHY area Part 1: Model and database.
709 Journal of Hydrology 217, 75-96.
710
711 Herschy, R.W., Fairbridge, R.W., 1998. Encyclopedia of Hydrology and Water Resources, 1st
712 ed., Kluwer Academic Publishers, 572-583.
713
714 Huffman, G.J. and Coauthors, 1997. The Global Precipitation Climatology Project (GPCP)
715 combined precipitation dataset. Bulletin of the American Meteorological Society 78, 5–20.
716
717 Kanamitsu, M., Ebisuzaki, W., Woollen, J., Yang, S.-K., 2002. NCEP/DOE AMIP-II
718 reanalysis (R-2). Bulletin of the American Meteorological Society 83, 1631–1643.
719
720 Manabe, S., Milly, P.C.D., Wetherald, R., 2004. Simulated long-term changes in river
721 discharge and soil moisture due to global warming. Hydrological Sciences Journal 49(4), 625-
722 642.
723
724 Masson, V., Champeaux, J.-L., Chauvin, F., Meriguet, C., Lacaze, R., 2002. A global
725 database of land surface parameters at 1-km resolution in meteorological and climate models.
726 Journal Of Climate 16(9), 1261-1282.
727
728 Meehl, G.A., Stocker, T.F., Collins, W.D., Friedlingstein, P., Gaye, A.T., Gregory, J.M.,
729 Kitoh, A., Knutti, R., Murphy, J.M., Noda, A., Raper, S.C.B., Watterson, I.G., Weaver, A.J.,
730 Zhao, Z.-C., 2007. Global Climate Projections. In: Climate Change 2007: The Physical
731 Science Basis. Contribution of Working Group I to the Fourth Assessment Report of the
732 Intergovernmental Panel on Climate Change [Solomon, S., D. Qin, M. Manning, Z. Chen, M.

733 Marquis, K.B. Averyt, M. Tignor and H.L. Miller (eds.)]. Cambridge University Press,
734 Cambridge, United Kingdom and New York, NY, USA.
735

736 Nohara, D., Kitoh, A., Hosaka, M., Oki, T., 2006. Impact of climate change on river discharge
737 projected by multimodel ensemble. *Journal of Hydrometeorology* 7(5), 1076-1089.
738

739 Noilhan, J., Lacarrère, P., 1995. GCM Grid-Scale Evaporation from Mesoscale Modeling.
740 *Journal of Climate* 8(2), 206–223.
741

742 Noilhan, J., Mahfouf, J.-F., 1996. The ISBA land surface parametrisation scheme. *Global and*
743 *Planetary Change* 13, 145-159.
744

745 Oki, T., Sud, Y.C., 1998. Design of Total Runoff Intergrating Pathways (TRIP) – A Global
746 River Channel Network. *Earth interactions* 2.
747

748 Pavelsky, T.M., Smith, L.C., 2004. Spatial and temporal patterns in Arctic river ice breakup
749 observed with MODIS and AVHRR time series. *Remote Sensing of Environment* 93, 328-
750 338.
751

752 Peters, D.L., Prowse, T.D., Pietroniro, A., Leconte, R., 2006. Flood hydrology of the Peace-
753 Athabasca Delta, northern Canada. *Hydrological Processes* 20, 4073-4096.
754

755 Peterson, B.J., Holmes, R.M., McClelland, J.W., Vörösmarty, C.J., Lammers, R.B.,
756 Shiklomanov, A.I., Shiklomanov, I.A., Rahmstorf, S., 2002. Increasing river discharge to the
757 Arctic Ocean. *Science* 298(5601), 2171–2173.

758

759 Pitman, A.J., Yang, Z-L., Cogley, J.G., Henderson-Sellers, A., 1991. Description of bare
760 essentials of surface transfer for the bureau of meteorology research centre AGCM. BMRC
761 Research Report No. 32, various pagings.

762

763 Prowse, T. D., 2001. River-ice ecology: I. Hydrologic, geomorphic, and water-quality aspects.
764 Journal of Cold Regions Engineering 15 (1), 1 – 16.

765

766 Rudolf, B., Hauschild, H., Reuth, W., Schneider, U., 1994. Terrestrial precipitation analysis:
767 Operational method and required density of point measurements. Global Precipitation and
768 Climate Change, M. Desbois and F. Desalmond, Eds., NATO ASI Series I 26, Springer-
769 Verlag, 173–186.

770

771 Serreze M. C., Bromwich, D.H., Clark, M.P., Etringer, A.J., Zhang, T., Lammers, R., 2002.
772 Large-scale hydro-climatology of the terrestrial Arctic drainage system. Journal of
773 Geophysical Research 108, doi:10.1029/2001JD000919.

774

775 Shiklomanov, A.I., Lammers, R.B., Vörösmarty, C.J., 2002. Widespread decline in
776 hydrological monitoring threatens panarctic research. EOS Transactions, American
777 Geophysical Union 83 (2), 13.

778

779 Smith, L.C., Alsdorf, D.E., 1998. Control on sediment and organic carbon delivery to the
780 Arctic Ocean revealed with space-borne synthetic aperture radar: Ob' River, Siberia. Geology
781 26 (5), 395-398.

782

783 Su, F.G., Adam, J.C., Trenberth, K.E., Lettenmaier, D.P., 2006. Evaluation of surface water
784 fluxes of the pan-Arctic land region with a land surface model and ERA-40 reanalysis.
785 Journal of Geophysical Research-Atmospheres 11, D5.
786

787 Versegny, D.L., 1991. CLASS - A Canadian land surface scheme for GCMs. I. Soil Model.
788 International Journal of Climatology 11, 111-133.
789

790 Vuglinsky, V.S., 2001. Peculiarities of ice events in Russian Arctic rivers. Hydrological
791 Processes 16, 905-913.
792

793 Wilson, M., Bates, P.D., Alsdorf, D., Forsberg, B., Horritt, M., Melack, J., Frappart, F.,
794 Famiglietti, J., 2007. Modeling large-scale inundation of Amazonian seasonally flooded
795 wetlands. Geophysical Research Letters 34, L15404, doi:10.1029/2007GL030156.
796

797 Wu, T., W., G., 2004. An empirical formula to compute snow cover fraction in GCMs.
798 Advances in Atmospheric Sciences 21, 529-535.
799

800 Yang, D., Ye, B., Shiklomanov, A., 2004. Discharge Characteristics and Changes over the Ob
801 River Watershed in Siberia. Journal of hydrometeorology 5, 595-610.
802

803 Yang, D., Zhao, Y., Armstrong, R., Robinson, D., Brodzik, M.-J., 2007. Streamflow response
804 to seasonal snow cover mass changes over large Siberian watersheds. Journal of Geophysical
805 Research 112, doi:10.1029/2006JF000518.
806

807 Yang, Z.-L., Dickinson, R.E., Robock, A., Vinnikov, K.Y., 1997. Validation of snow sub-
808 model of the biosphere-atmosphere transfer scheme with Russian snow-cover and
809 meteorological observations data. *Journal of Climate* 10, 353-373.

810 Table captions

811

812 Table 1. GSWP2 experiments with the reanalysis used as precipitation forcing and the applied

813 correction(s)

814

815 Table 2. Correlation coefficient, bias, RMSE and Nash-Sutcliffe coefficient between

816 measured and modelled discharge at Salekhard for different precipitation datasets and for

817 $c_{pn}=0.01$, $w_{drain}=0.02$ and Z_{0new}

818

819 Table 3. Correlation coefficient and Nash-Sutcliffe coefficient between modelled and in-situ

820 discharge at Salekhard for different values of the river depth (m) and the Manning coefficient

821 (bold numbers correspond to GSWP2-P4 and non-bold numbers correspond to GSWP2-P3)

822

823 Table 4. Mean RMSE between Topex/POSEIDON and modelled water heights for GSWP2-

824 P3 and GSWP2-P4

Figure captions

Fig. 1. Study domain (Lower Ob). The red arrows represent the lateral inflows to the hydraulic model, the green arrow represents the boundary condition (from the Belogorje gauging station), the blue line represents the water mask used to describe the river in the hydraulic model

Fig. 2. Models used in this study and their interactions (LISFLOOD-FP is a flood inundation model, ISBA is a Land Surface Scheme and TRIP is a routing scheme)

Fig. 3. Routing scheme used to compute the lateral inflows to the river from the ISBA study domain (the lateral inflow number, see Fig. 1, is indicated in red). The blue dots represent the pixels on the lower Ob and the yellow dots, each ISBA grid cell which contributes to the lateral inflow

Fig. 4. River bathymetry (red curve) computed from a filtered topography (magenta curve) derived from the ACE DEM elevation along the river (blue dots)

Fig. 5. DEMs available on the study domain: GTOPO30 (from USGS) and ACE (from De Montfort University). The ACE DEM has been chosen for our study.

Fig. 6. In-situ discharge at Belogorje with a time lag of 10 days and in-situ discharge at Salekhard with no time-lag; their difference gives an estimate of the total lateral inflow to the river between the two gages (a.). This "in-situ" total lateral inflow is compared to the sum of the ISBA lateral inflows (b.). The eight modelled lateral inflows are also shown (c.)

850

851 Fig. 7. Modelled lateral inflow $n^{\circ}6$ from ISBA (blue dashed line on all plots) compared to
852 (red curves) rain precipitation rate (a.), snow precipitation rate (b.), evapotranspiration (c.),
853 snow fraction (d.), air temperature (e.), temperature in the first soil layer (f.), liquid water
854 equivalent soil ice (g.) and soil liquid water (h.). These plots correspond to a spatial average
855 on all ISBA grid cells contributing to lateral inflow $n^{\circ}6$ (see Fig. 3)

856

857 Fig. 8. Soil/vegetation roughness length (Z_0) and vegetation cover (VEG) averaged for all the
858 ISBA grid cells contributing to lateral inflow 6 (a.). Modelled snow fraction on vegetation
859 (p_{nc}) and on bare soil (p_{ng}) are also shown (b.)

860

861 Fig. 9. Total lateral inflow from in-situ measurement (cyan curve) compared to modelled total
862 lateral inflow for c_{pn} equal to 5, 1, 0.1, 0.01 and 0.001 and for roughness length equal to Z_0
863 (a.) and Z_{0new} (b.)

864

865 Fig. 10. Sum of modelled lateral inflows for $w_{drain}=0, 0.01, 0.02, 0.03$ and 0.05 with
866 $c_{pn}=0.01$ and roughness length equal to Z_{0new}

867

868 Fig. 11. Sum of all lateral inflows for all the GSWP2 precipitation datasets for $c_{pn}=5$,
869 $w_{drain}=0$ and Z_0 (nominal run, a.) and for $c_{pn}=0.01$, $w_{drain}=0.02$ and Z_{0new} (b.). Modelled
870 discharge at Salekhard for all the GSWP2 precipitation datasets for $c_{pn}=5$, $w_{drain}=0$ and Z_0
871 (c.) and for $c_{pn}=0.01$, $w_{drain}=0.02$ and Z_{0new} (d.)

872

873 Fig. 12. Modelled discharge at Salekhard for different values of the river depth (5m, 10m and
874 15m) and for a Manning coefficient of 0.015 (a. and c.). Modelled discharge at Salekhard for

875 different values of the Manning coefficient (0.01, 0.015, 0.02 and 0.025) and for a river depth
876 of 10m (b. and d.). Plots a. and b. are obtained with lateral inflows computed using GSWP2-
877 P3 precipitation field, whereas plots c. and d. are obtained with GSWP2-P4 precipitation
878 dataset. On each plot, the blue curve corresponds to the observed discharge at Salekhard
879

880 Fig. 13. Location of the different Topex/Poseidon virtual stations used

881

882 Fig. 14. Comparison between Topex/POSEIDON measured water height (red curves on the
883 two plots) and modelled water height with GSWP2-P3 (magenta dashed curve) and with
884 GSWP2-P4 (black curve) for a river depth of 10m and a Manning coefficient of 0.015 at the
885 location of virtual stations n°4 (a.), n°9 (b.), n°17 (c.) and n°24 (d.) (see Fig. 13 for their
886 location)

887 Table 5 :
888

GSWP2 experiment	Reanalysis	Hybridization	Gauge correction
B0	NCEP/DOE	Yes (GPCC and GPCP)	Yes
P1	ERA-40	No	No
P2	NCEP/DOE	Yes (GPCC)	Yes
P3	NCEP/DOE	Yes (GPCC)	No
P4	NCEP/DOE	No	No
PE	ERA-40	Yes (GPCC and GPCP)	No

889 Table 2:
890

Precipitation ISBA input	Model vs observation			
	Correlation coefficient	Bias (m ³ /s)	RMSE (m ³ /s)	Nash-Sutcliffe coefficient
GSWP2-B0	0.97	-1571	3 554	0.88
GSWP2-P1	0.99	700	2 157	0.96
GSWP2-P2	0.96	-2797	5 183	0.75
GSWP2-P3	0.99	674	1 917	0.97
GSWP2-P4	0.99	-1363	2 289	0.95
GSWP2-PE	0.98	-912	2 607	0.94

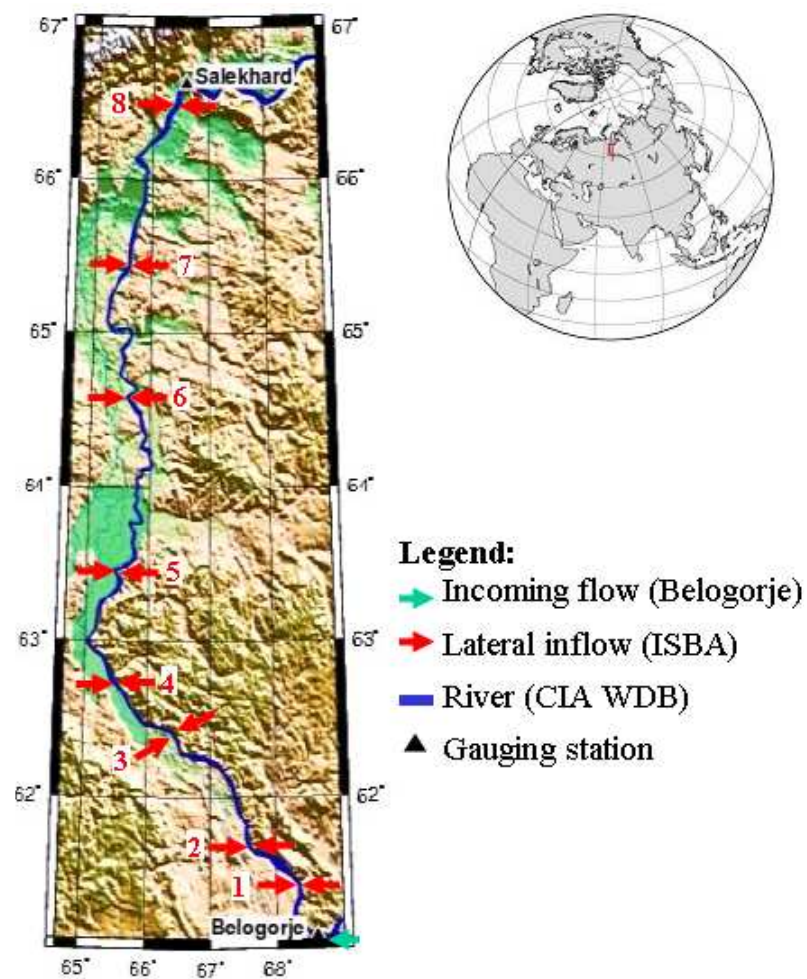
891 Table 3:
892

River depth (m)	Manning coefficient	Correlation coefficient	RMSE (m ³ /s)	Nash- Sutcliffe
5	0.01	0.86 0.88	5 393 5 310	0.74 0.75
	0.015	0.56 0.59	8 920 8 924	0.28 0.28
	0.02	0.25 0.30	10 982 11 032	-0.09 -0.10
	0.025	-0.0002 0.06	12 105 12 029	-0.32 -0.30
10	0.01	0.98 0.96	2 263 3 510	0.95 0.89
	0.015	0.99 0.99	2 136 2 409	0.96 0.95
	0.02	0.89 0.88	4 861 5 248	0.79 0.75
	0.025	0.71 0.70	7 423 7 833	0.50 0.45
15	0.01	0.98 0.95	2 508 3 951	0.94 0.86
	0.015	0.98 0.97	2 131 3 405	0.96 0.90
	0.02	0.99 0.98	1 956 2 722	0.97 0.93
	0.025	0.98 0.98	2 489 2 595	0.94 0.94

893 Table 4:
894

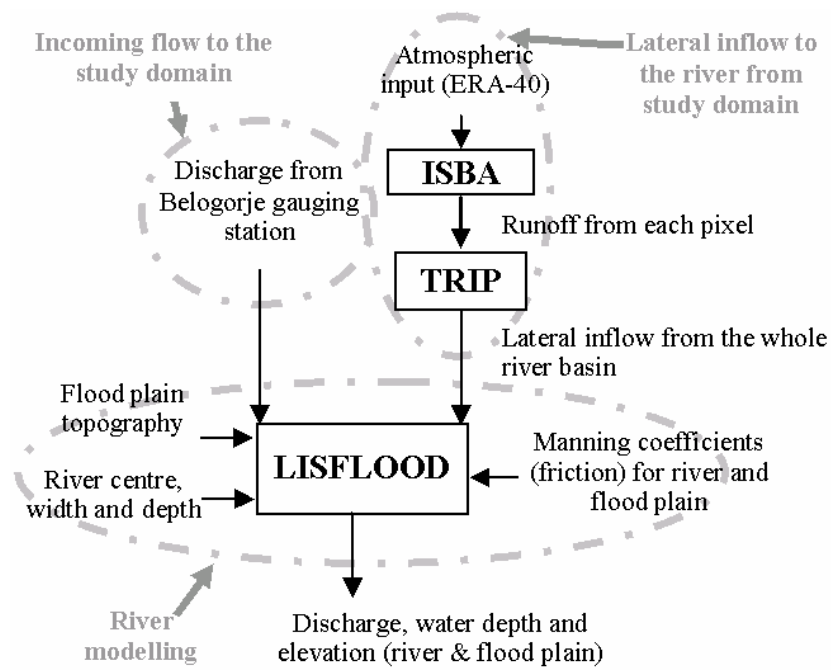
Precipitation	Topex station	Mean RMSE modelled/Topex water height (m)	
		RD=10m Cman=0.015	RD=15m Cman=0.020
GSWP2-P3	All stations	2.6	5.7
	Station n°4	1.7	4.4
	Station n°9	2.3	4.9
	Station n°17	2.0	5.1
	Station n°24	3.2	6.2
GSWP2-P4	All stations	2.0	4.6
	Station n°4	1.1	3.5
	Station n°9	1.6	3.9
	Station n°17	1.2	4.0
	Station n°24	2.2	5.0

895 Figure 1:
896



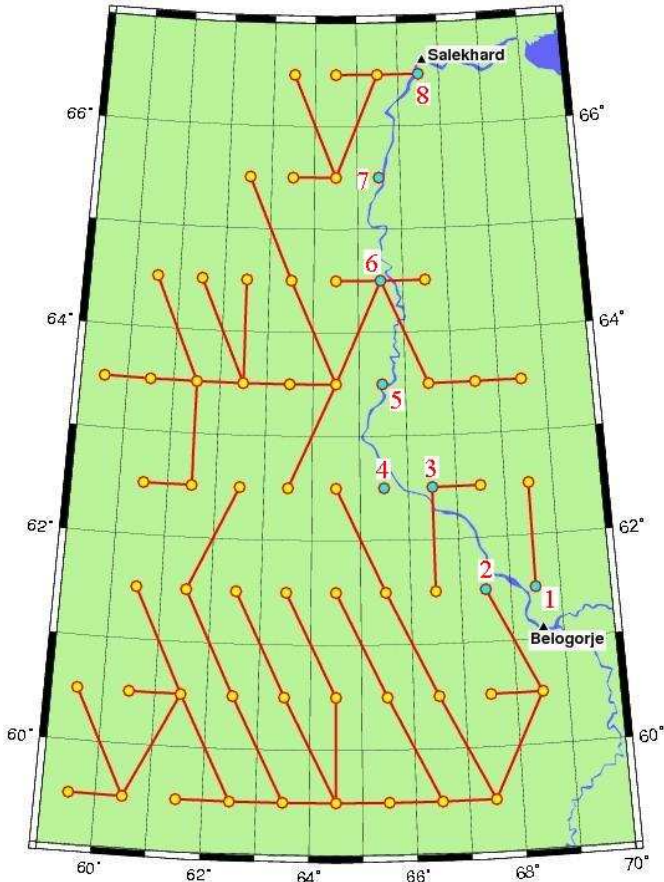
897

898 Figure 2:
899



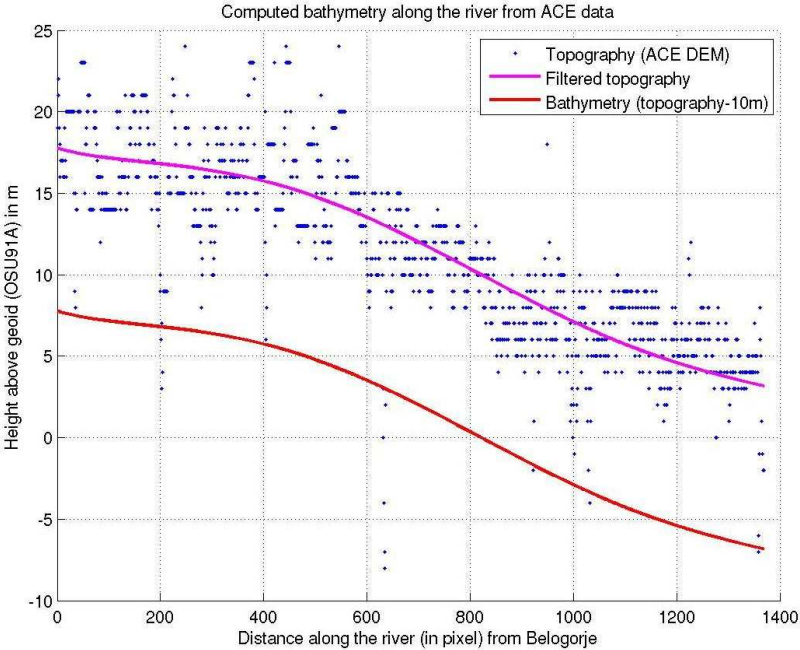
900

901 Figure 3:
902



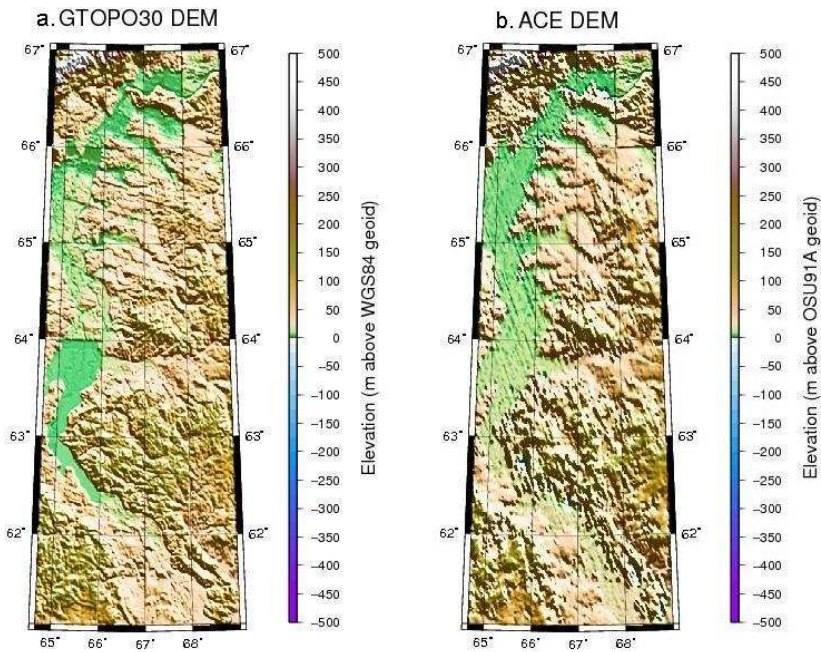
903

904 Figure 4:
905



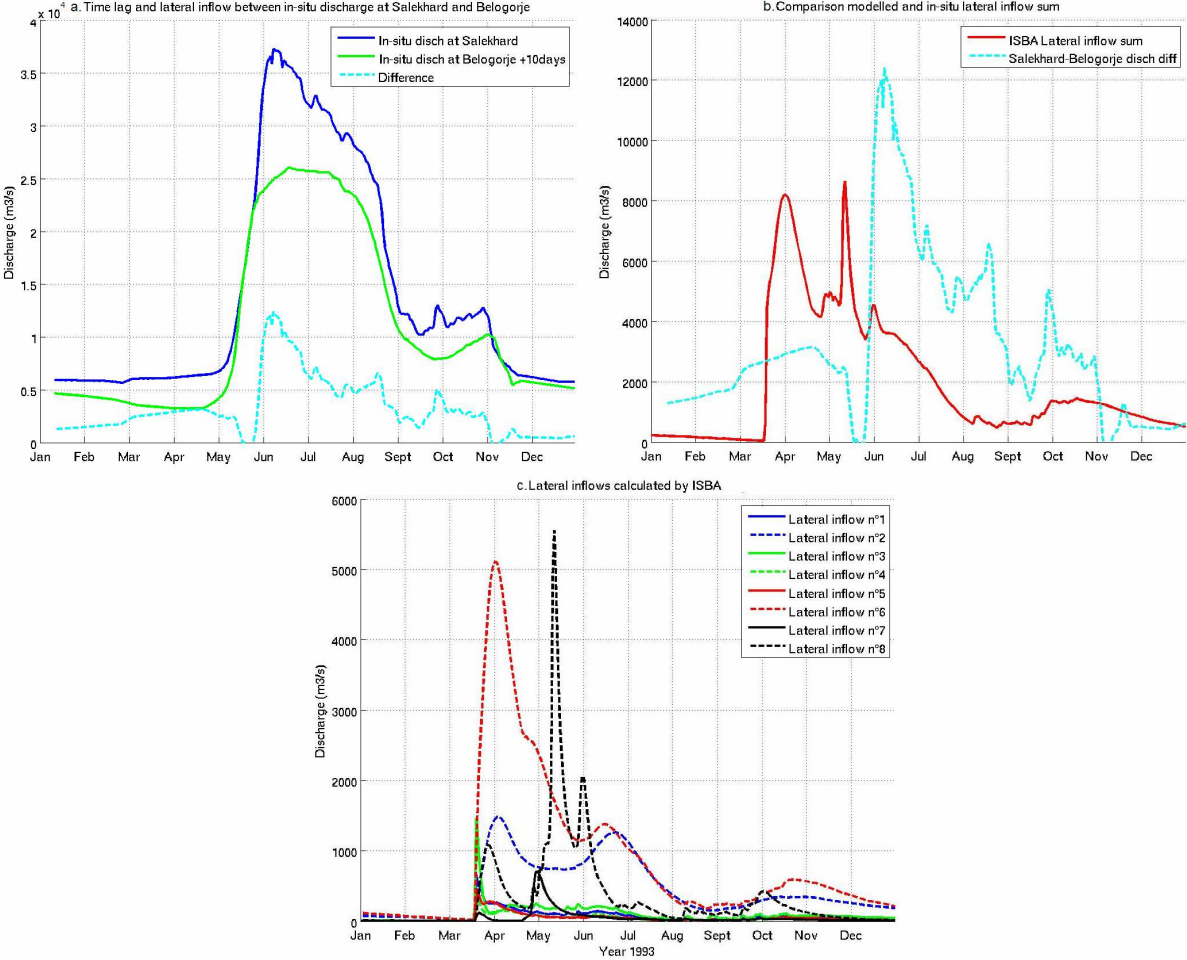
906

907 Figure 5:
908



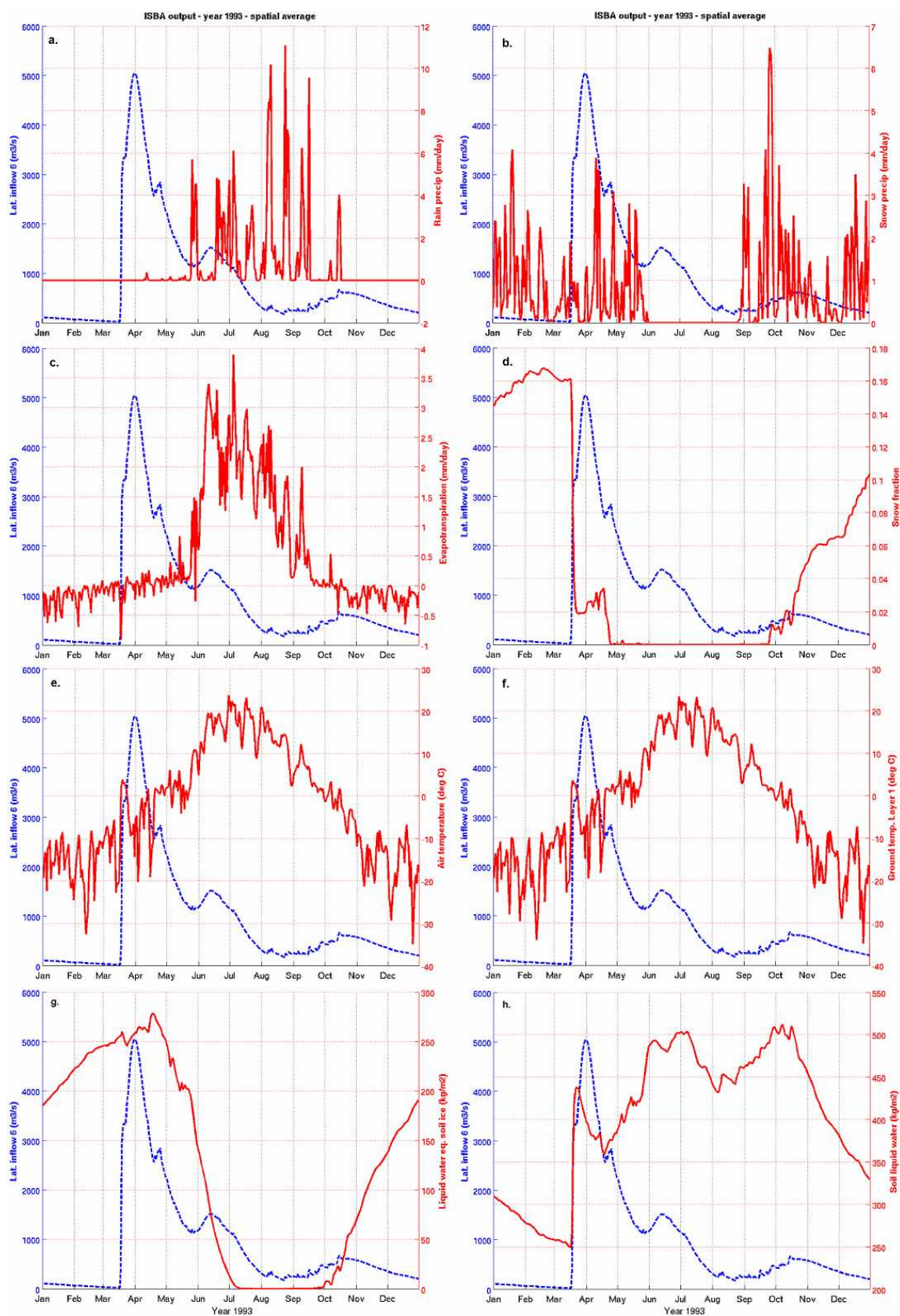
909

910 Figure 6:
911



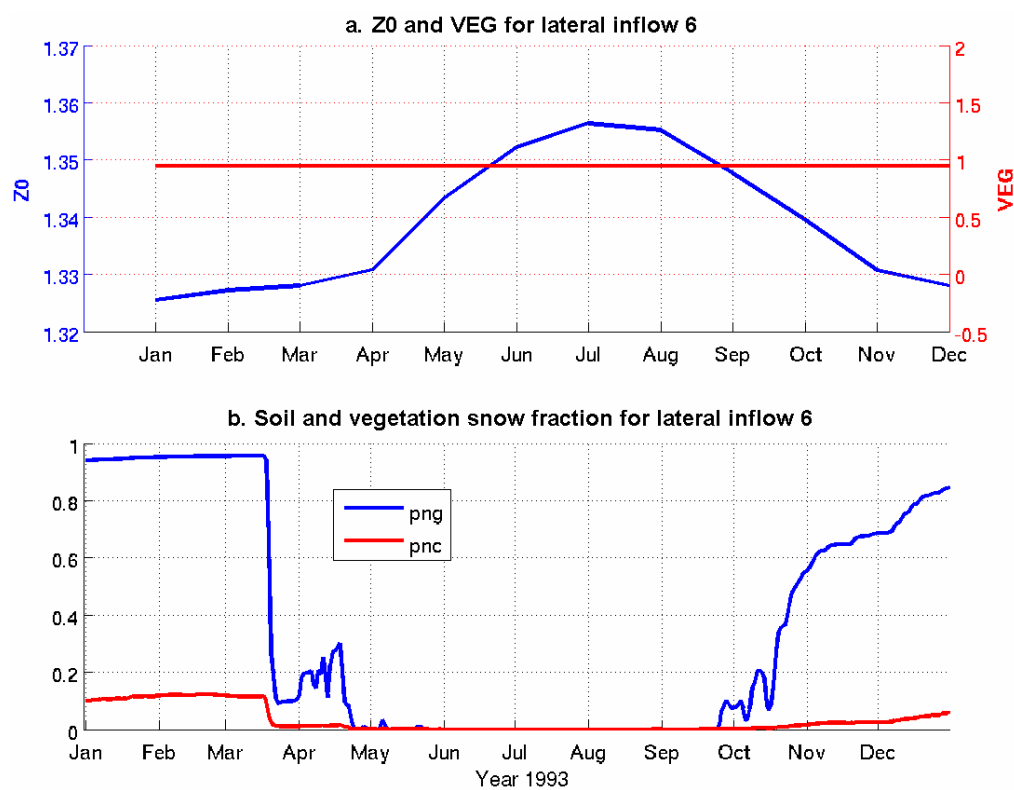
912

913 Figure 7:
914



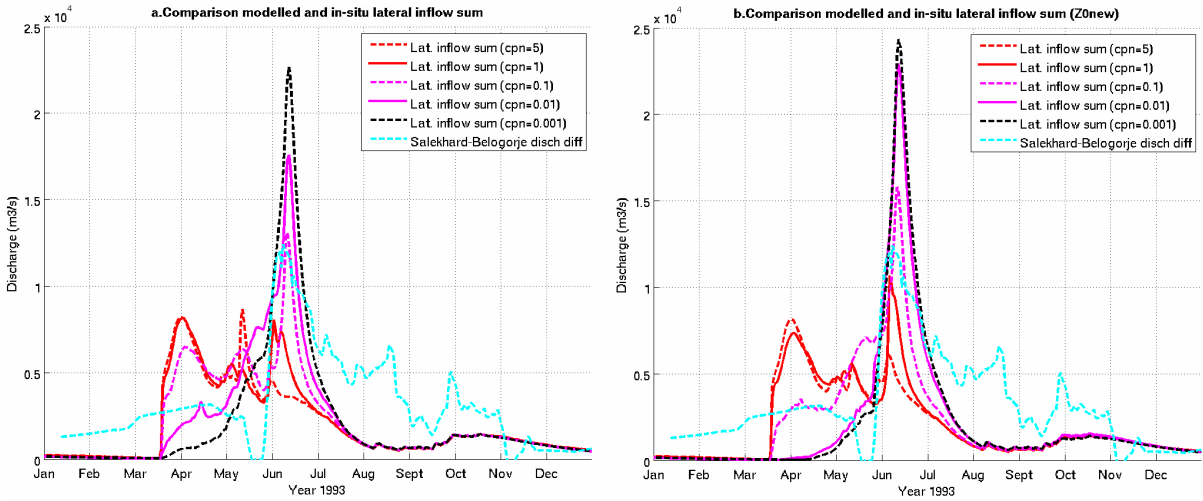
915

916 Figure 8:
917

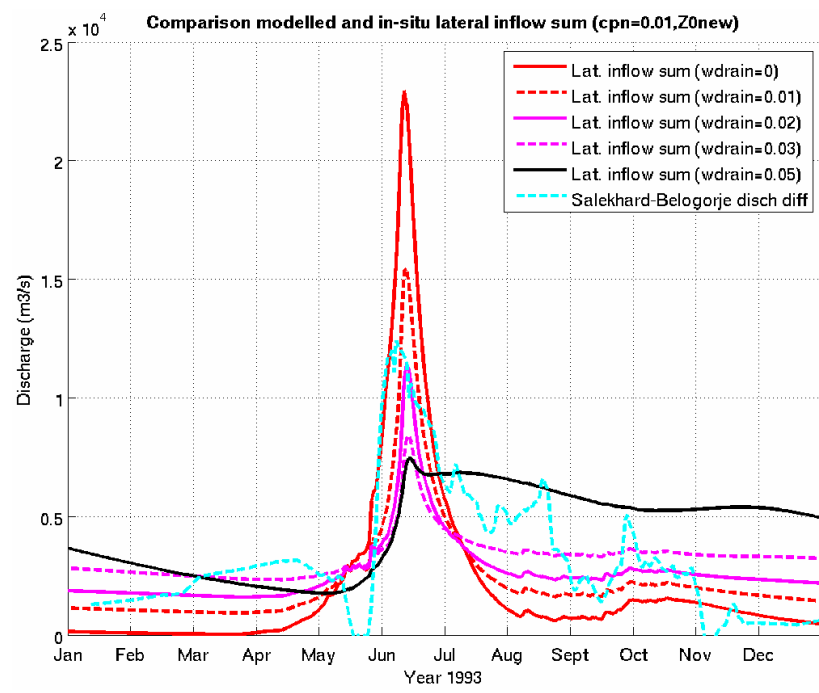


918
919

Figure 9:

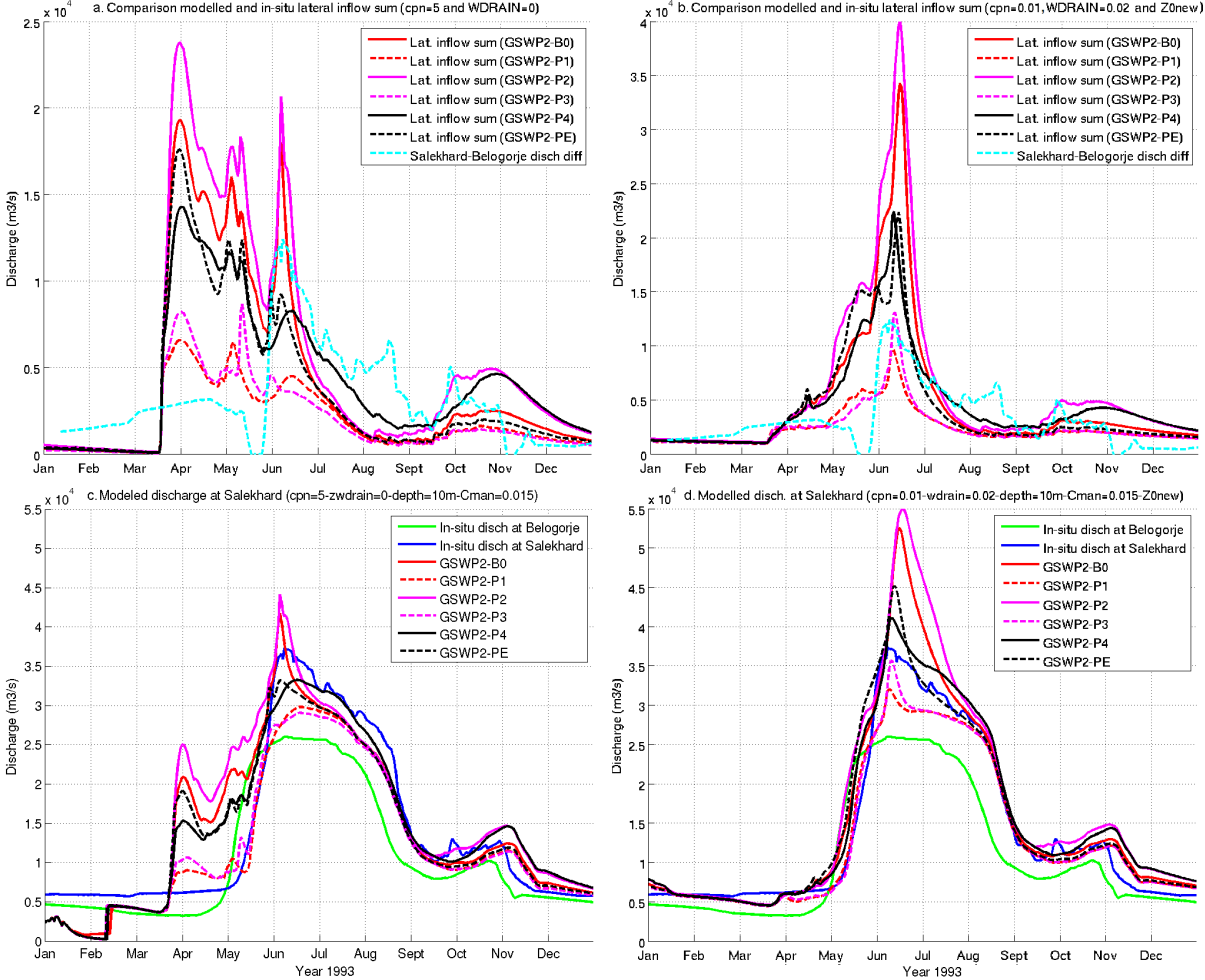


924 Figure 10:
925



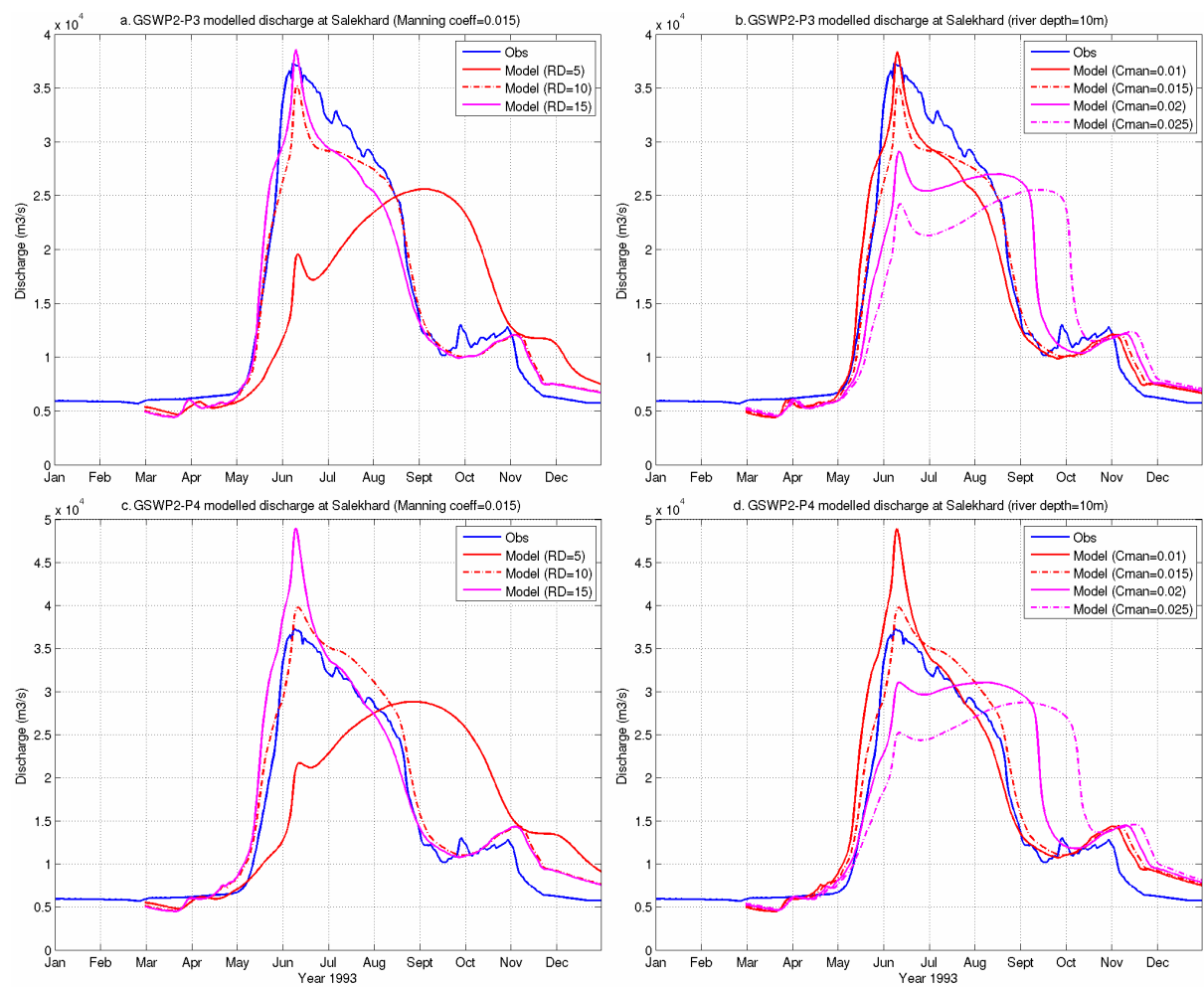
926

927 Figure 11:
928



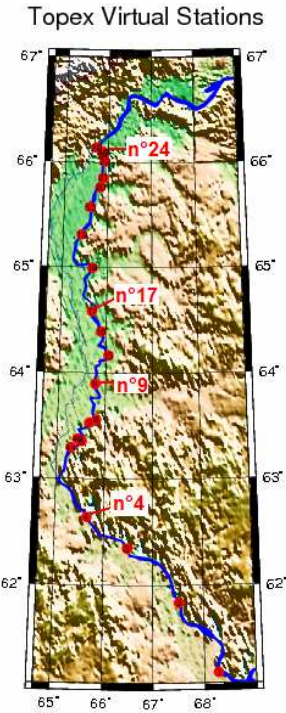
929

930 Figure 12:
931



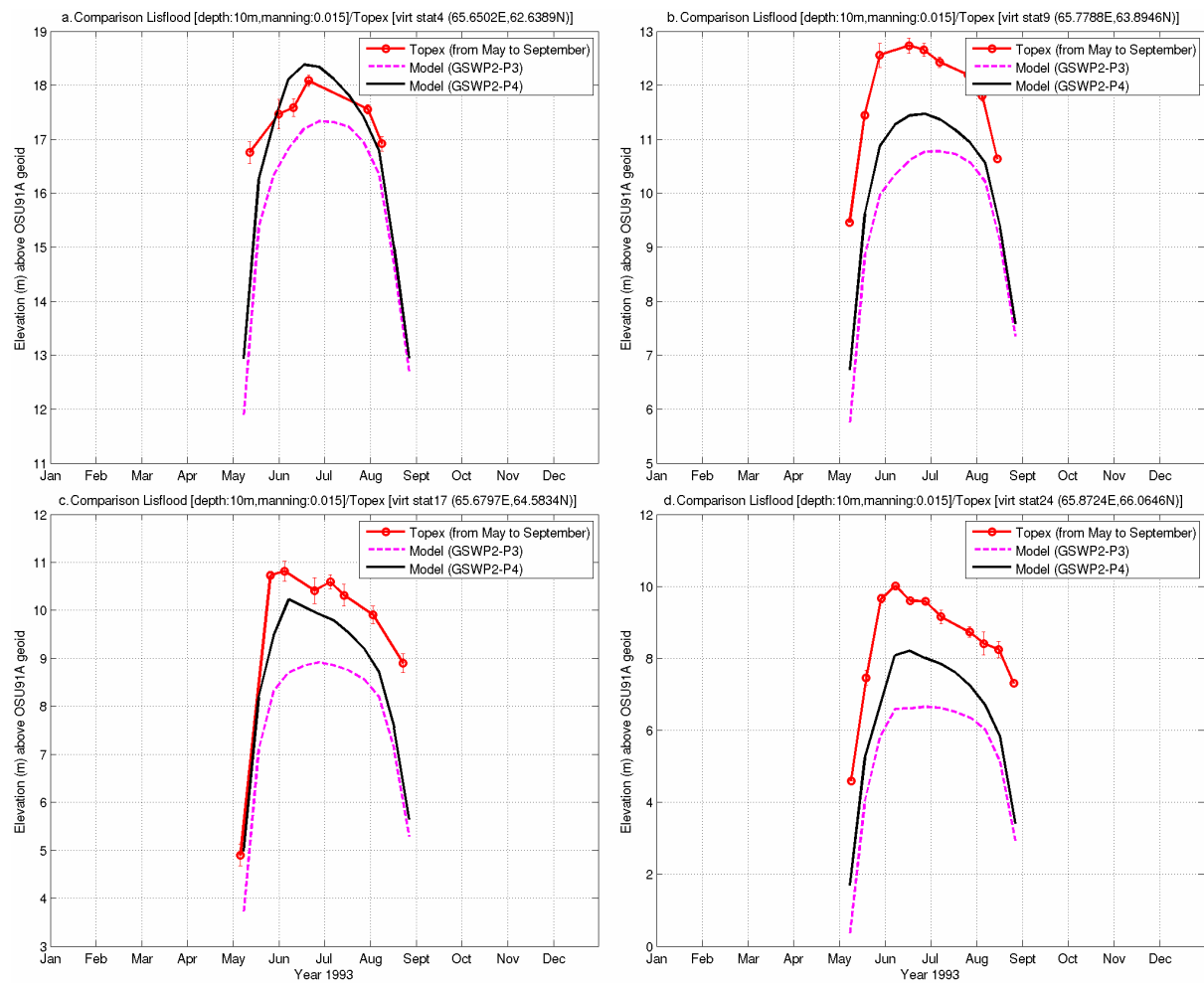
932

933 Figure 13:
934



935

936 Figure 14:
937



938
939